Int. J. Electrochem. Sci., 8 **(2013)** 6281 - 6290

International Journal of
ELECTROCHEMICAL
SCIENCE
www.electrochemsci.org

Characteristics of $ZnMn_2O_4$ Nanopowders Prepared by Flame Spray Pyrolysis for Use as Anode Material in Lithium Ion Batteries

Seung Ho Choi, Yun Chan Kang[*]

Department of Chemical Engineering, Konkuk University, 1 Hwayang-dong, Gwangjin-gu, Seoul 143-701, Korea
[*]E-mail: yckang@konkuk.ac.kr

Received: 25 February 2013 / *Accepted:* 6 April 2013 / *Published:* 1 May 2013

$ZnMn_2O_4$ nanopowders with homogeneous composition are prepared by flame spray pyrolysis from an aqueous spray solution containing Zn and Mn components. The $ZnMn_2O_4$ powders subjected to post-treatment at 500°C exhibit a mean size of 65 nm and nonaggregation characteristics. The discharge capacities of the precursor powder and the $ZnMn_2O_4$ powders post-treated at 400, 500, and 600°C are 1156, 1230, 1192, and 1086 mAh g^{-1}, respectively, after 40 cycles at a current density of 300 mA g^{-1}, and the corresponding capacity retentions measured after the first cycle are 69, 75, 78, and 79%. The $ZnMn_2O_4$ nanopowders post-treated at 500°C exhibit high initial discharge and charge capacities of 1192 and 632 mAh g^{-1}, respectively, at a current density of 1000 mA g^{-1}. The discharge capacity of the powders decreases from 1192 to 470 mAh g^{-1} during the first 15 cycles, and then becomes stable at values above 450 mAh g^{-1} until 110 cycles. Subsequently, the discharge capacities of the $ZnMn_2O_4$ nanopowders increase gradually from the 110^{th} cycle onward. The maximum discharge capacity reaches 670 mAh g^{-1} after 160 cycles.

Keywords: nanoparticles; flame spray pyrolysis; zinc manganate; anode material

1. INTRODUCTION

Various transition metal oxides such as Fe_2O_3, Co_3O_4, Mn_2O_3, and NiO have attracted much attention as anode materials for lithium ion batteries (LIBs) because of their high theoretical capacities [1-6]. The combination of two types of transition metal oxides in an AB_2O_4 spinel-like structure has been widely studied as a promising anode material with high capacity and good cycle performance in LIBs [7-10]. Because powder size and morphology strongly affect the capacity and cycling performance of these transition metal oxides [11-13], research on the structures of various

multicomponent transition metal oxides prepared using well-developed solid-state and liquid solution methods has been carried out [7-10].

Zinc manganite ($ZnMn_2O_4$) is one of the most attractive compounds of the AB_2O_4 series because of its low oxidation potential and low material cost [14]. The electrochemical properties of various $ZnMn_2O_4$ structures such as nanopowders, nanowires, hollow microspheres, and ball-in-ball microspheres have been investigated [10,14-18]. These nano-structured $ZnMn_2O_4$ materials have been prepared primarily by liquid solution methods such as sol-gel, coprecipitation, hydrothermal, and solvothermal processes.

Gas-phase reaction methods have also been applied to the preparation of various types of anode materials for LIBs [19-26]. Spray pyrolysis had advantages in the preparation of metal oxide powders with complex compositions because of the microscale reactions that take place within droplets that are several microns in size [21,22]. Flame spray pyrolysis, in which a high-temperature flame is applied as an energy source for the drying and decomposition of metal salts, has been applied in the preparation of anode nanopowders for LIBs, and it is thought that flame spray pyrolysis could easily be commercialized for large-scale production of metal oxide nanopowders by continuous process [23-26]. Metal oxide nanopowders with simple compositions such as Co_3O_4, Sn/SnO_2 prepared by flame spray pyrolysis have been studied as anode materials [23,24]. However, to the best of our knowledge, using high-temperature flame spray pyrolysis to fabricate multicomponent transition metal oxides for anode application in LIBs has not been studied.

In this study, $ZnMn_2O_4$ nanopowders with homogeneous composition were directly prepared by flame spray pyrolysis from an aqueous spray solution of Zn and Mn components. The electrochemical properties of the precursor powder and the post-treated $ZnMn_2O_4$ nanopowders at high current densities were investigated.

2. EXPERIMENTAL

$ZnMn_2O_4$ nanopowders were directly prepared by flame spray pyrolysis. The system had a droplet generator, flame nozzle, powder collector, and blower [27]. A 1.7 MHz ultrasonic spray generator with six resonators was used to generate droplets, which were then carried into the high-temperature diffusion flame using oxygen as the carrier gas. The diffusion flame was generated using propane as the fuel and oxygen as the oxidizer. The flame nozzle had five concentric pipes. Droplets generated from the precursor solution were supplied to the diffusion flame through the center pipe by the carrier gas. The flow rates of fuel, oxidizer, and carrier gases were 5, 40, and 10 L min^{-1}, respectively. The spray solutions were obtained by dissolving zinc nitrate hexahydrate [$Zn(NO_3)_2 \cdot 6H_2O$, Junsei, 97%] and manganese nitrate tetrahydrate [$Mn(NO_3)_2 \cdot 4H_2O$] into distilled water. The overall concentration of tin and copper components was fixed at 0.5 M.

The crystal structures of the prepared powders were investigated using X-ray diffractometry (XRD, X'pert PRO MPD) with Cu Kα radiation (λ = 1.5418 Å) at the Korea Basic Science Institute (Daegu). Morphological characteristics were investigated using *high-resolution transmission electron microscopy* (TEM, JEOL-2100F). The capacities and cycle properties of the powders were determined

using a 2032-type coin cell. The anode electrode was prepared from a mixture containing 75 wt% active material, 15 wt% Super P® carbon black as the conductive material, and 10 wt% sodium carboxymethyl cellulose (CMC) as the binder. Lithium metal and microporous polypropylene film were used as the counter electrode and separator, respectively. $LiPF_6$ (1 M) in a mixture of ethylene carbonate (EC) and dimethyl carbonate (DMC) in a 1:1 volume ratio with 2 wt% vinylene carbonate (VC) was used as the electrolyte (Techno Semichem Co.). The charge/discharge characteristics of the samples were determined through cycling in the voltage range 0.001–3 V at different current densities. Cyclic voltammetry measurements were carried out at a scan rate of 0.07 mV s^{-1}.

3. RESULTS AND DISCUSSION

The crystal structure of the precursor powders directly prepared by flame spray pyrolysis is shown in Fig. 1.

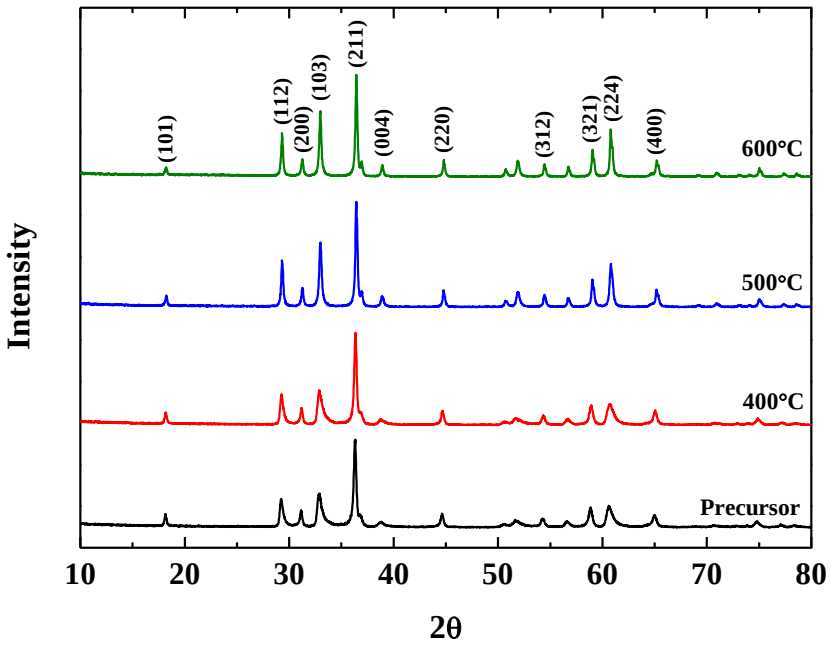

Figure 1. X-ray diffraction patterns of the $ZnMn_2O_4$ precursor and powders post-treated at 400, 500, and 600°C.

The precursor powders exhibited a phase-pure $ZnMn_2O_4$ structure without impurity phases. The post-treatment of the precursor powders improved the sharpness of the XRD patterns of the $ZnMn_2O_4$ powders shown in Fig. 1. The mean crystallite sizes of the $ZnMn_2O_4$ precursor powder and the powders post-treated at 400, 500, and 600°C were 44, 56, 65, and 74 nm, respectively, as calculated from the half-width of the (211) XRD peak using Scherrer's equation.

The morphologies of the precursor powders directly prepared by flame spray pyrolysis are shown in Fig. 2. As shown in the low-resolution TEM images, the $ZnMn_2O_4$ powders had nanometer-

sized particles and displayed nonaggregation characteristics. Submicron- or micron-sized powders formed directly from droplets several microns in size were not observed. The high-resolution TEM image (Fig. 2b) shows a crystalline polyhedral structure.

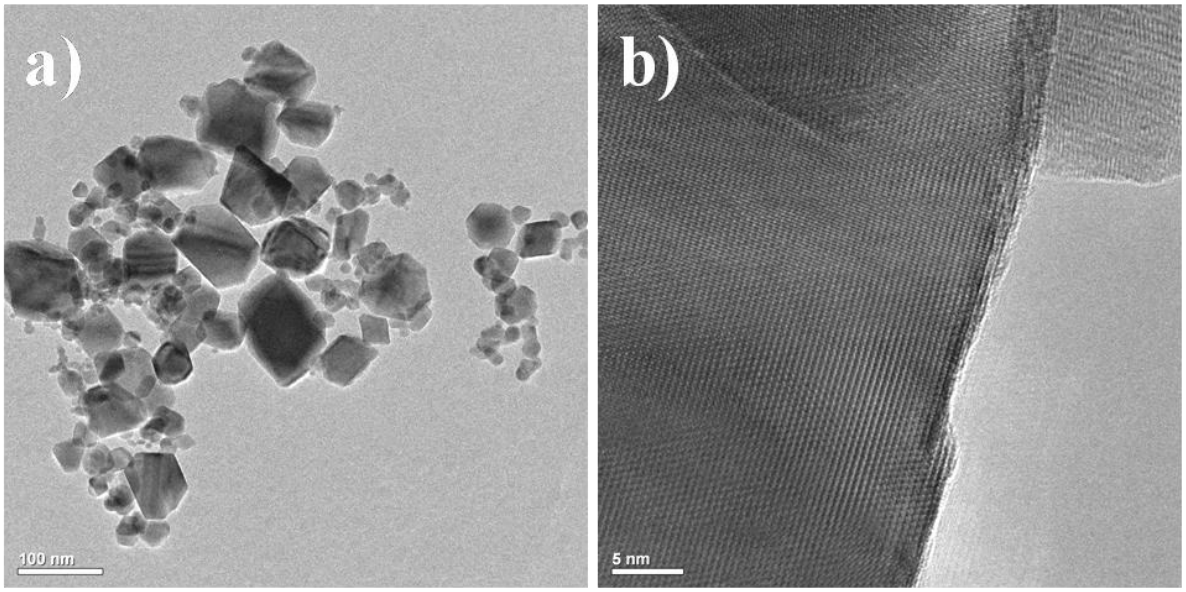

Figure 2. Low and high resolution TEM images showing the precursor $ZnMn_2O_4$ nanopowders.

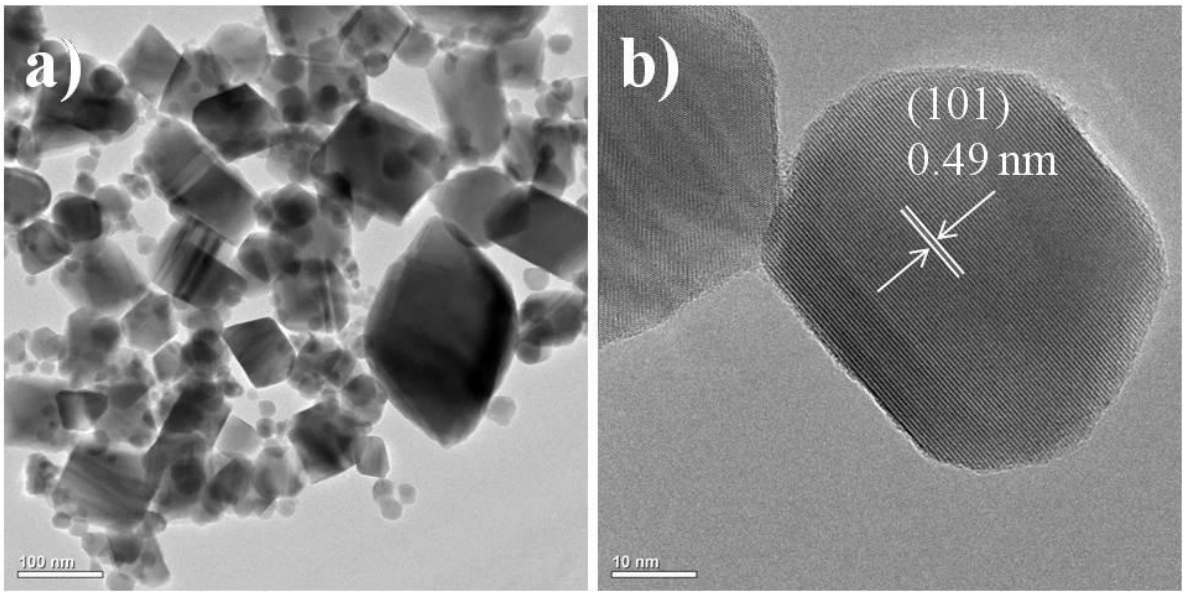

Figure 3. Low and high resolution TEM images showing the $ZnMn_2O_4$ nanopowders post-treated at 500°C.

The drying and decomposition of a droplet inside the high-temperature diffusion flame formed a micron-sized composite powder consisting of Zn and Mn components. The Zn and Mn components

completely evaporated in the high-temperature diffusion flame to form vapors of zinc and manganese oxides. Nanocomposite oxide powders of Zn and Mn components were formed from the vapors by nucleation and growth processes. The immediate reaction and crystallization of zinc and manganese oxides formed crystalline $ZnMn_2O_4$ powders even with the short residence time of the powders in the high-temperature diffusion flame. The prepared $ZnMn_2O_4$ powders had well-faceted polygonal shapes. The high temperature of the diffusion flame and the high cooling rate of the powders produced metastable polymorphs [28].

The morphologies of the $ZnMn_2O_4$ powders post-treated at a temperature of 500°C are shown in Fig. 3. The powders post-treated at 500°C were in the nanometer scale, similar to the precursor powders directly prepared by flame spray pyrolysis. The low- and high-resolution TEM images (Figs. 3a and b) show that the post-treated $ZnMn_2O_4$ powders exhibited nonaggregation characteristics. The high-resolution TEM image of the powders exhibited clear lattice fringes separated by 0.49 nm and a single-phase crystalline structure. This value corresponds to the (101) plane of the $ZnMn_2O_4$ [18]. The mean size of the post-treated powders as measured from the low-resolution TEM images was 65 nm.

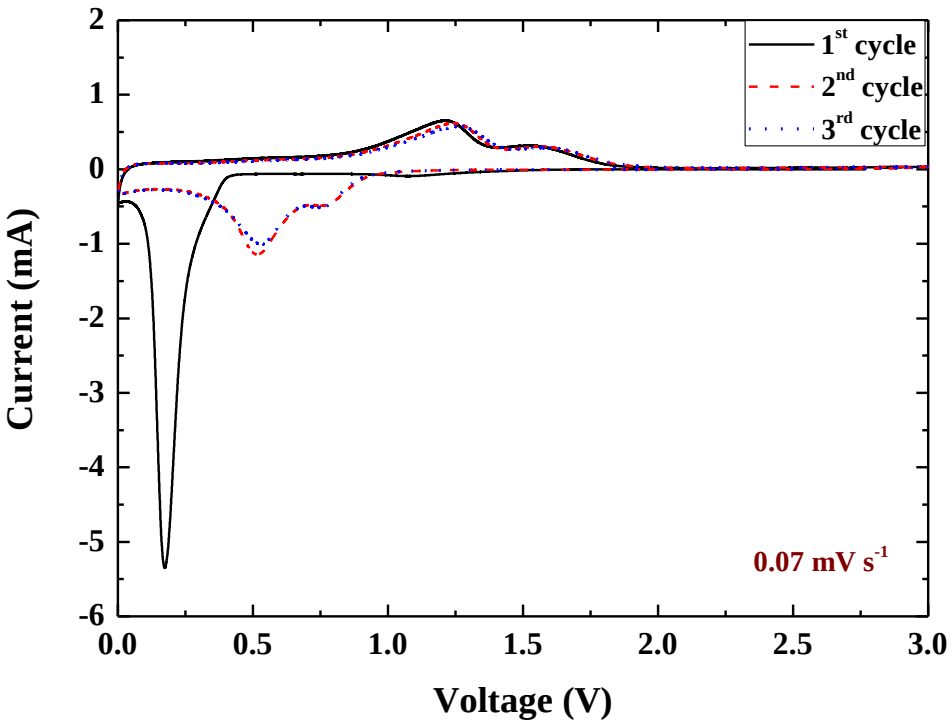

Figure 4. Cyclic voltammograms of the $ZnMn_2O_4$ nanopowders post-treated at 500°C at a scan rate of 0.07 mV s^{-1} in the voltage range of 0.001–3 V.

Fig. 4 shows the cyclic voltammograms (CVs) of the single-crystalline $ZnMn_2O_4$ powders post-treated at 500°C during the first, second, and third cycles at a scan rate of 0.07 mV s^{-1} in the voltage range 0.001–3 V. The CVs of the $ZnMn_2O_4$ powders showed features similar to those of Mn_2O_3 and ZnO [10,14]. An intensive reduction peak at ~0.2 V was observed in the first cycle, which may be attributed to the irreversible reduction of $ZnMn_2O_4$ with concomitant crystal structure destruction to

form metallic nanograins (Zn^0, Mn^0) dispersed in an amorphous Li_2O matrix [10]. The first charge sweep showed two oxidation peaks at approximately 1.2 and 1.5 V, which could be associated with the oxidation of metallic Zn and Mn nanograins to ZnO (1.5 V) and Mn_2O_3 (1.2 V), respectively [14,29]. From the second cycle onward, the reduction/oxidation peaks in the CV tests overlap very well, indicating that the electrode fabricated from the $ZnMn_2O_4$ nanopowders shows good cyclability for the insertion and extraction of lithium ions.

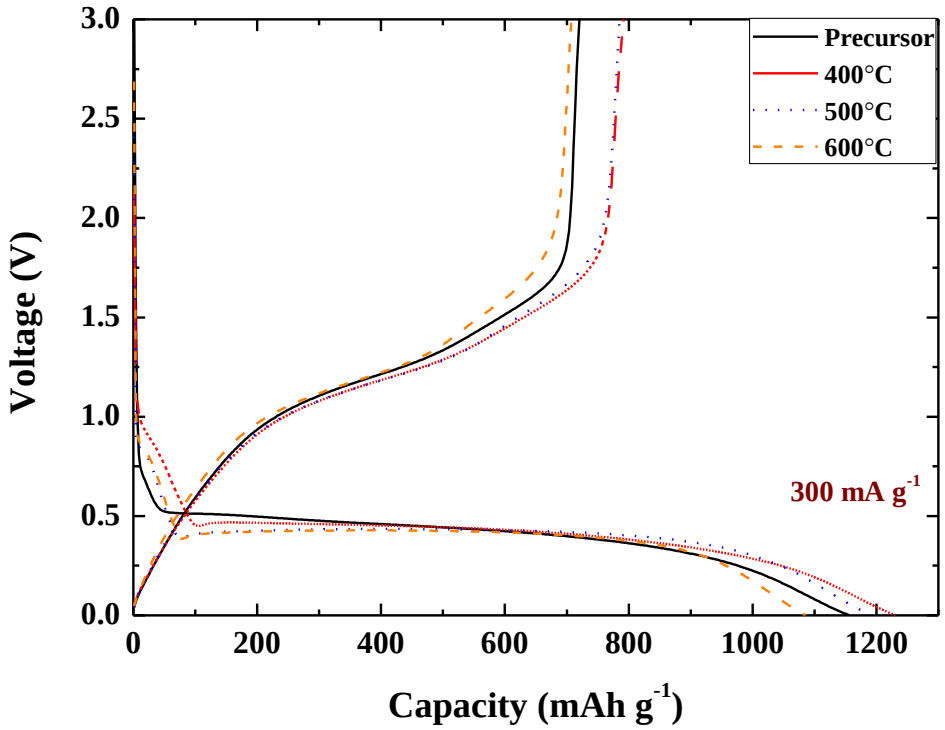

Figure 5. First charge and discharge curves of the $ZnMn_2O_4$ precursor powder and the powders post-treated at 400, 500, and 600°C at a constant current density of 300 mA g^{-1}.

Fig. 5 shows the initial charge and discharge curves of the $ZnMn_2O_4$ precursor powder and the powders post-treated at 400, 500, and 600°C at a constant current density of 300 mA g^{-1}. The charge and discharge curves of the post-treated $ZnMn_2O_4$ powders had similar shapes, irrespective of the post-treatment temperature. In the initial discharge curves, all the $ZnMn_2O_4$ powders showed one plateau at 0.4 V, which can be attributed to the reduction of $ZnMn_2O_4$ into metallic manganese and zinc, as shown in the intensive reduction peak in the CV curve of the first cycle. The initial discharge capacities of the $ZnMn_2O_4$ precursor powder and the powders post-treated at 400, 500, and 600°C were 1156, 1230, 1191, and 1086 mAh g^{-1}, respectively, and the charge capacities were 720, 791, 785, and 707 mAh g^{-1}, respectively. The $ZnMn_2O_4$ nanopowders post-treated at 400 and 500°C had higher initial charge and discharge capacities than did the precursor powders prepared directly by flame spray pyrolysis. The Coulombic efficiencies of the $ZnMn_2O_4$ nanopowders post-treated at 400 and 500°C in the first cycle were 64 and 66%, respectively. The irreversible capacity loss of the $ZnMn_2O_4$

nanopowders in the first cycle can be attributed to the formation of a solid electrolyte interphase film and the decomposition of the electrolyte [14,30,31].

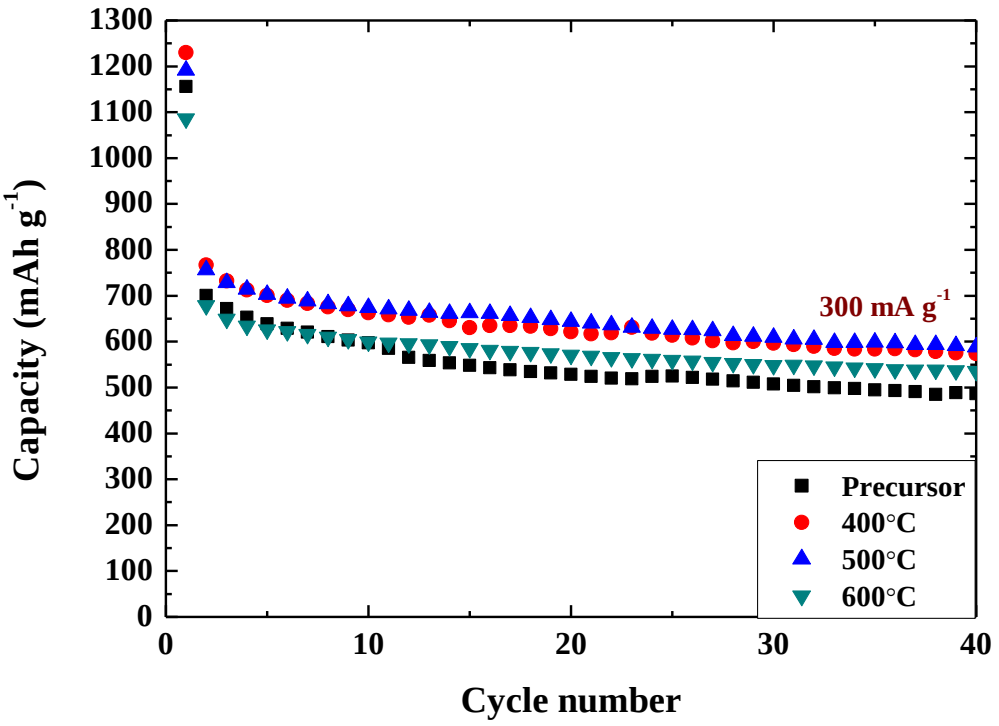

Figure 6. Cycle performances of the $ZnMn_2O_4$ precursor powder and the powders post-treated at 400, 500, and 600°C at a constant current density of 300 mA g^{-1}.

Fig. 6 shows the cycle properties of the $ZnMn_2O_4$ precursor powder and the powders post-treated at 400, 500, and 600°C at a constant current density of 300 mA g^{-1}. The discharge capacities of the precursor powder and the $ZnMn_2O_4$ powders post-treated at 400, 500, and 600°C were 1156, 1230, 1192, and 1086 mAh g^{-1}, respectively, after 40 cycles, and the corresponding capacity retentions measured after the first cycle were 69, 75, 78, and 79%. The post-treatment of the powders improved the cycling performances of the $ZnMn_2O_4$ nanopowders. Phase homogeneity and high crystallinity improved the cycling performance and the initial charge and discharge capacities of the post-treated $ZnMn_2O_4$ nanopowders. The particle growth and aggregation between the nanopowders decreased the electrochemical properties of the $ZnMn_2O_4$ powders post-treated at 600°C. Fig. 7 shows the TEM and dot-mapping images and XRD patterns of the $ZnMn_2O_4$ powders after the 40^{th} cycle with a fully charged state. The size and shape of the $ZnMn_2O_4$ nanopowders were maintained after cycling. However, the angular edges of the nanopowders became smooth after cycling, and the crystalline structure was not observed in the high-resolution TEM image, as shown in Fig. 7b. The crystalline $ZnMn_2O_4$ phase completely transformed into an amorphous-like phase after cycling. The dot-mapping images of the $ZnMn_2O_4$ powders after cycling, as shown in Fig. 7c, show the homogeneous composition of the powders, in which a phase separation of Zn and Mn components was not observed. The Zn and Mn components were uniformly distributed throughout the nanopowder after cycling. The

XRD pattern of the electrode after cycling, as shown in Fig. 7c, did not show the crystalline structures of the Zn and Mn components. The peaks corresponding to the copper foil were only observed in the XRD pattern of the electrode. The transition of the crystalline structure of $ZnMn_2O_4$ into an amorphous one during cycling has been reported in previous studies [10].

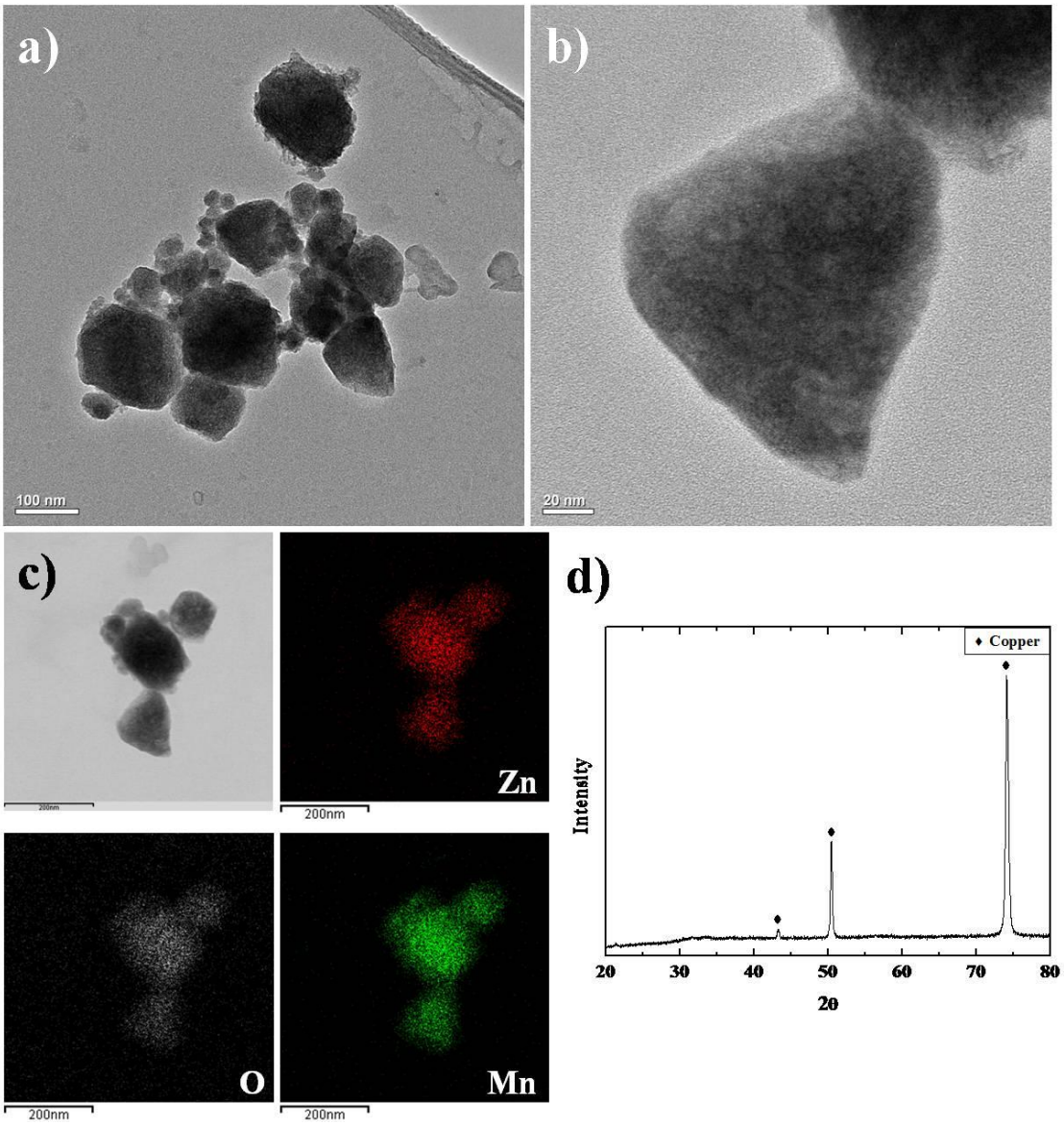

Figure 7. TEM and dot-mapping images and XRD patterns of the $ZnMn_2O_4$ powders after the 40th cycle with a fully charged state.

The rate performance of the $ZnMn_2O_4$ nanopowders post-treated at 500°C is shown in Fig. 8. These nanopowders exhibited high initial discharge and charge capacities of 1192 and 632 mAh g^{-1}, respectively, at a current density of 1000 mA g^{-1}. The Coulombic efficiency of the first cycle was only 65%. However, the Coulombic efficiency steadily increased with increasing cycle number, and high efficiencies above 99% were maintained from the 6th cycle onward. The discharge capacity of the powders decreased from 1192 to 470 mAh g^{-1} during the first 15 cycles, thereafter maintaining stable

discharge capacities above 450 mAh g^{-1} up to 110 cycles. The discharge capacities of the $ZnMn_2O_4$ nanopowders then increased gradually from the 110th cycle onward. The maximum discharge capacity of 670 mAh g^{-1} was reached after 160 cycles.

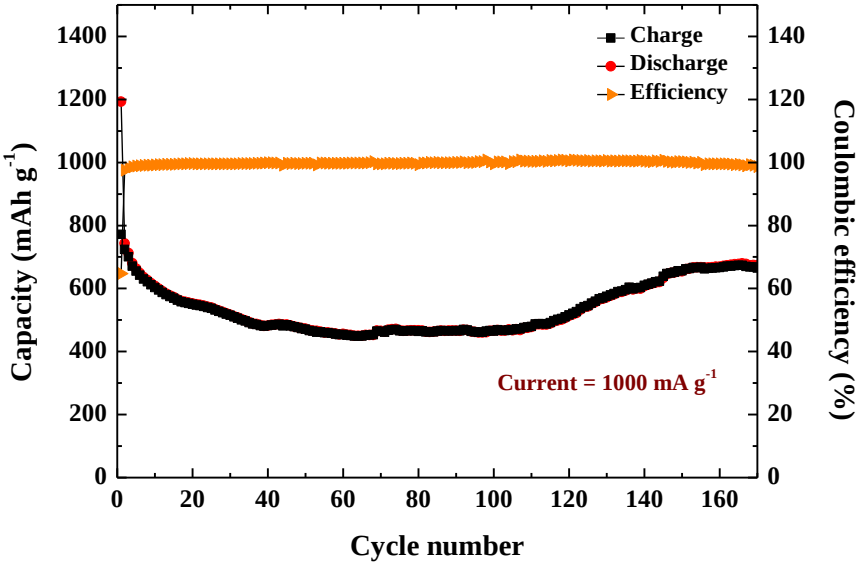

Figure 8. Rate performance of the $ZnMn_2O_4$ nanopowders post-treated at 500°C at a constant current density of 1000 mA g^{-1}.

The reason for the increase in discharge capacity during cycling was estimated to be the result of the formation of a polymeric gel-like film on the active material [14,15,32]. The increase in discharge capacity during cycling has also been observed in $ZnMn_2O_4$ prepared by a thermally driven contraction process and the co-precipitation method [14,15].

4. CONCLUSIONS

The electrochemical properties of the $ZnMn_2O_4$ precursor powder and the nanopowders obtained by flame spray pyrolysis and subsequent post-treatment were investigated at high current densities. The precursor powders had a phase-pure $ZnMn_2O_4$ structure without impurity phases. The post-treatment of the precursor powders improved the sharpness of the XRD pattern of the $ZnMn_2O_4$ powders. The powders post-treated at 500°C were in nanometer scale, similar to the precursor powders. The $ZnMn_2O_4$ nanopowders post-treated at 500°C had higher initial charge and discharge capacities than did the precursor powders. Phase homogeneity and high crystallinity improved the cycling performance and the initial charge and discharge capacities of the post-treated $ZnMn_2O_4$ nanopowders. The maximum discharge capacity of the $ZnMn_2O_4$ powders post-treated at 500°C reached 670 mAh g^{-1} after 160 cycles at a current density of 1000 mA g^{-1}.

ACKNOWLEDGEMENT
This paper resulted from the Konkuk University research support program.

References

1. Z. Y. Wang, L. Zhou, X. W. Lou, *Adv. Mater.*, 24 (2012) 1903.
2. C. H. Jiang, E. J. Hosono, H. S. Zhou, *Nanotoday*, 1 (2006) 28.
3. N. R. Kang, J. H. Park, J. W. Choi, J. W. Jin, J. S. Chun, I. G. Jung, J. H. Jeong, J. G. Park, S. M. Lee, H. J. Kim, S. U. Son, *Angew. Chem. Int. Ed.*, 51 (2012) 6626.
4. Y. M. Sun, X. L. Hu , W. Luo, F. F. Xia, Y. H. Huang, *Adv. Funct. Mater.*, (2012) DOI: 10.1002/adfm.201202623.
5. H. G. Cha, J. H. Sohn, Y. J. Park, K. J. Lee, M. H. Jung, J. W. Lee, W. S. Shin, M. J. Kang, D. Y. Kim, Y. S. Kang, *RSC Adv.*, 2 (2012) 9786.
6. Z. S. Wu, W. C. Ren, L. Wen, L. B. Gao, J. P. Zhao, Z. P. Chen, G. M. Zhou, F. Li, H. M. Cheng, *ACS Nano*, 4 (2010) 3187.
7. M. V. Reddy, C. Yu, F. Jiahuan, K. P. Loh, B. V. R. Chowdari, *RSC Adv.*, 2(2012) 9619.
8. B. Liu, J. Zhang, X. F. Wang, G. Chen, D. Chen, C. W. Zhou, G. Z. Shen, *Nano Lett.*, 12 (2012) 3005.
9. Y. Wang, D. W. Su, A. Ung, J. H. Ahn, G. X. Wang, *Nanotechnology*, 23 (2012) 055402.
10. S. W. Kim, H. W. Lee, P. Muralidharan, D. H. Seo, W. S. Yoon, D. K. Kim, K. S. Kang, *Nano Res.*, 4 (2011) 505.
11. C. J. Kim, M. J. Noh, M. S. Choi, J. P. Cho, B. W. Park, *Chem. Mater.*,17 (2005) 3297.
12. J. F. Ye, H. J. Zhang, R. Yang, X. G. Li, L. M. Qi, S*mall*, 6 (2010) 296.
13. H. B. Wu, J. S. Chen, H. H. Hng, X. W. Lou, *Nanoscale*, 4 (2012) 2526.
14. F. M. Courtel, H. Duncan, Y. Abu-Lebdeh, I. J. Davidson, *J. Mater. Chem.*, 21 (2011) 10206.
15. G. Q. Zhang, L. Yu, H. B. Wu, H. E. Hoster, X. W. Lou, *Adv. Mater.*, 4 (2012) 4609.
16. L. F. Xiao, Y. Y. Yang, J. Yin, Q. Li, L. Z. Zhang, *J. Power Sources*, 194 (2009) 1089.
17. Y. F. Deng, S. D. Tang, Q. M. Zhang, Z. C. Shi, L. T. Zhang, S. Z. Zhana, G. H. Chen, *J. Mater. Chem.*, 21 (2011) 11987.
18. L. Zhou, H. B. Wu, T. Zhu, X. W. Lou, *J. Mater. Chem.*, 22 (2012) 827.
19. M. M. Rahman, S. L. Chou, C. Zhong, J. Z. Wang, D. Wexler, H. K. Liu, *Solid State Ionics*, 180 (2010) 1646.
20. Y. N. Ko, J. H. Kim, S. H. Choi, Y. C. Kang, *J. Power Sources*, 211 (2012) 84.
21. Y. N. Ko, Y. C. Kang, S. B. Park, *Int. J. Electrochem. Sci.*, 8 (2013) 2504.
22. S. H. Ju, Y. C. Kang, *J. Phys. Chem. Solids*, 70 (2009) 40.
23. Y. A. Kim, Y. S. Yoon, D. W. Shin, *Solid State Ionics*, 192 (2011) 308.
24. Y. A. Kim, Y. S. Yoon, D. W. Shin, *J. Anal. Appl. Pyrolysis*, 85 (2009) 557.
25. S. H. Ng, T. J. Patey, R. Büchel, F. Krumeich, J. Z. Wang, H. K. Liu, S. E. Pratsinis, P. Novák, *Phys. Chem. Chem. Phys.*, 11 (2009) 3748.
26. T. J. Patey, S. H. Ng, R. Büchel, N. Tran, F. Krumeich, J. Wang, H. K. Liu, P. Novák, *Electrochem. Solid-State Lett.*, 11 (2008) A46.
27. S. H. Choi, Y. N. Ko, J. H. Kim, Y. J. Hong, Y. C. Kang, *J. Alloys Compd.*, 509 (2011) 7979.
28. R. Strobel, S. E. Pratsinis, *J. Mater. Chem.*, 17 (2007) 4743.
29. Y. Sharma, N. Sharma, G. V. S. Rao, B. V. R. Chowdari, *Adv. Funct. Mater.*, 17 (2007) 2855.
30. J. Xin, C. Jia-jia, X. Jian-hui, S. Yi-ning, F. You-zuo, Z. Min-sen, D. Quan-feng, *Chem. Commun.*, 48 (2012) 7410.
31. G. Binotto, D. Larcher, A. S. Prakash, R. H. Urbina, M. S. Hegde, J. M. Tarascon, *Chem. Mater.*, 19 (2007) 3032.
32. G. M. Zhou, D. W. Wang, F. Li, L. L. Zhang, N. Li, Z. S. Wu, L. Wen, G. Q. Lu, H. M. Cheng, *Chem. Mater.*, 22 (2010) 5306.